AIAA JOURNAL
Vol. 44, No. 6, June 2006

Fiber-Optic Wall Shear Gauge for Hot High-Speed Flows

Matthew W. Orr* and Joseph A. Schetz†
Virginia Polytechnic Institute and State University, Blacksburg, Virginia 24061
and
Robert S. Fielder‡
Luna Innovations, Inc., Blacksburg, Virginia 24060

This investigation details the design, analysis, and testing of a new, two-component wall shear gauge for three-dimensional, high-temperature flows. This gauge is a direct-measuring, nonnulling design with a round head surrounded by a small gap. Two flexure rings are used to allow small motions of the floating head. Strain gauges are mounted on the flexures, and fiber-optic displacement sensors measure how far polished faces of counterweights move in relation to a fixed housing. The strain gauges are for validation of the newer fiber optics. The sensor is constructed of Haynes® 230®, a high-temperature nickel alloy. All components, in pure fiber-optic form, can survive to a temperature of 1073 K. The dynamic range of the sensor is from 0–500 Pa. Higher shear forces can be measured by changing the floating head size. No damping or water cooling of the sensor is required. Finite element modeling was used during the design and analysis of the sensor. Static structural, modal, and thermal analyses were performed using the ANSYS finite element package. Repeated cold-flow tests at Mach 2.4 and Mach 4.0 under high-Reynolds-number conditions have been accomplished in the Virginia Tech Supersonic Wind Tunnel. Experimental results are in excellent agreement with semiempirical prediction methods.

Nomenclature

C_f	=	skin-friction coefficient
n	=	normal to wall
P	=	pressure
Pr	=	Prandtl number
Re	=	Reynolds number
r	=	recovery factor
T	=	temperature
U_e	=	edge velocity
u^*	=	friction velocity
V	=	velocity
δ	=	boundary-layer thickness
μ	=	viscosity
ρ	=	density
σ	=	standard deviation
τ	=	shear

Subscripts

w	=	wall
0	=	stagnation condition

Introduction

THE drag of any object moving through a fluid can be broken up into two primary components: the pressure drag and the viscous drag. Measuring both quantities is important for vehicle, as well as engine, performance prediction and analysis. This study focuses on the measurement of viscous drag in supersonic flows.

The wall shear drag is the streamwise component of shear force integrated over the whole vehicle, and the definition for a local value in a Newtonian fluid is shown in Eq. (1). The skin-friction coefficient shown in Eq. (2) is a convenient dimensionless form of the local wall shear:

$$\tau_w = \mu \left.\frac{\partial V}{\partial n}\right|_w \tag{1}$$

$$C_f = \frac{\tau_w}{\frac{1}{2}\rho_e U_e^2} \tag{2}$$

Another important quantity is the friction velocity, Eq. (3). The friction velocity is a way of normalizing parameters to show the influence of the wall shear. For turbulent flows, the friction velocity is an important correlating quantity that yields results such as the law of the wall[1]:

$$u_* = \sqrt{\tau_w/\rho_e} = U_e\sqrt{C_f/2} \tag{3}$$

There are two broad categories of sensor types that are used to measure the wall shear.[2,3] The first type directly senses the wall shear. The second broad category measures another flow quantity and uses assumed relationships to infer the value of the shear at the wall. These methods are known as direct and indirect, respectively. Direct methods are preferred for complex, especially three-dimensional, flows because the correlations needed for indirect methods are nonexistent or inaccurate for complex flow cases.

The goal of this research is to develop a direct-measuring wall shear sensor capable of operating at temperatures up to 1073 K and measuring two components of the wall shear, in the plane of the wall, for three-dimensional flows. Fiber-optic displacement sensors and associated bonding techniques were chosen as they can survive in the harsh 1073 K design conditions. In addition, fiber-optic sensors are much less sensitive to temperature changes than strain gauges. Past studies have used conventional strain gauges to measure the wall shear.[4,5] Other studies have used fiber-optic inferometry to measure the displacement of a floating head, but only for low-temperature applications.[6] This study uses both measurement devices for redundancy and also validation of the newer fiber-optic sensors.

Presented as Paper 2004-0545 at the AIAA 42nd Aerospace Sciences Meeting, Reno, NV, 5–8 January 2004; received 17 February 2004; revision received 6 July 2005; accepted for publication 16 August 2005.

*Graduate Assistant, Department of Aerospace and Ocean Engineering; currently Configuration Design Engineer, Boeing Commercial Airplanes, Seattle, WA 98124. Member AIAA.

†Fred D. Durham Chair, Department of Aerospace and Ocean Engineering. Fellow AIAA.

‡Director, Optical Devices Group.

Wall shear is a small quantity compared with other forces in the flow, 250 Pa distributed over a 16-mm-diam circle in a Mach 2.4 flow is only 0.01257 N (0.00128 kg or 0.00282 lb). When a supersonic wind tunnel starts, the static pressure in the test section goes from atmospheric to a low level in a fraction of a second. A gauge must be able to survive such a violent change in conditions and still be sensitive enough to measure the wall shear with reasonable accuracy. This extremely sensitive force measurement device must also be insensitive to changes in temperature, pressure gradients, or other possible influences.

The design goal of this gauge is to be able to operate at 1073 K indefinitely. The design shear level of 250 Pa was selected as this is representative of hot, high-speed flows, and this level can be achieved in local wind-tunnel facilities. A wide range of shear values can be measured as the sensor design allows the sensing area to be changed, that is, a larger floating head for smaller shear values and a smaller head for flows with higher shear values.

Design Background

The history of direct-measuring skin-friction gauges is described in a special Web page (www.aoe.vt.edu/~jschetz/Skin_Friction/Cf_Gage_Table&Refs.pdf [cited 27 July 2004]) compiled at Virginia Tech. Several previous wall shear gauge designs used a single cantilever-beam flexure with a floating head on the top[6–8] (see Fig. 1). For laboratory applications, the gauge can be filled with a viscous fluid for damping and thermal protection. Several designs have used semiconductor strain gauges that are about 100 times more sensitive than metal foil strain gauges, but they are also much more sensitive to changes in temperature. The second method of measurement for this type of gauge was to measure the tilt of the displaced head with fiber-optic displacement sensors.[6] Success with this concept was mixed as the gauge was sensitive to vibration at high frequencies, and this caused difficulty with the fiber-optic measurement systems when no internal damping fluid was used.

Previous investigations have demonstrated a need for damping. This can be accomplished with the use of a damping fluid or with other materials.[7] A novel method of using rubber sheets as a damping and isolation material has been investigated, but this method is impractical for high-temperature applications as rubber sheets are incapable of the needed temperatures.[8] Viscous damping is less desirable for optical shear gauges as it adds one more level of complexity to the problem. There are issues with the index of refraction of the damping fluid and its change with temperature.[6] The high shear deflection required by metal-foil strain gauges can induce a large misalignment error between the head of the sensor and the housing even though they are less sensitive to temperature changes than semiconductor strain gauges.

When examining past shear gauges, one flexure concept stood out from the rest as the best choice for a gauge that could combine both fiber optics and metal-foil strain gauges into a single package for redundancy and validation. A wheel with flexible spokes has been chosen as the best candidate for the flexure of this new gauge. This general type of skin-friction sensor was developed for use in the X-43 flight-test vehicle.[9] It used conventional strain gauges and an aluminum flexure. This design was for a very limited duration test, and more exotic materials were not needed. That gauge was also limited to sensing a single component of shear. A key feature of this design concept is that the flexure is mass balanced, and this makes the gauge less susceptible to vibrations and linear accelerations. This work extends this flexure concept to measure two components of wall shear and adds the ability to use fiber-optic displacement sensors.

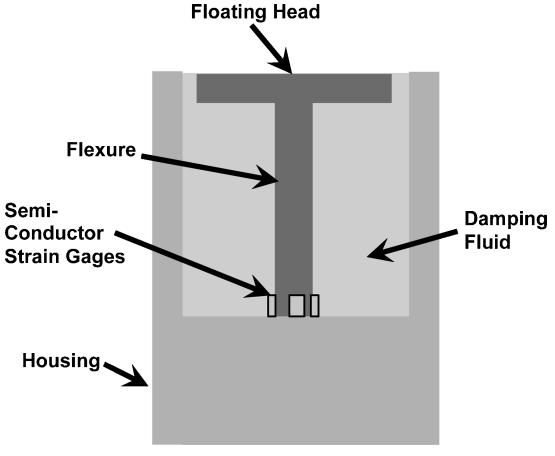

Fig. 1 Schematic of prior shear gauge concepts.

Gauge Description

Figure 2 shows the current design, which is a two-component wheel-flexure gauge. Both the streamwise and transverse shear components can be measured in a three-dimensional flow. In both concepts, the spokes of the wheels are very thin beams. These beams are weak in the direction of rotation, and they are strong in the directions where motion is not desired. These spokes are the only parts of both gauges that are designed to flex. The X-shear arrow on the sensing head will cause motion in the lower wheel assembly, and this is the first and primary component of the shear force measured. These arrows show the direction of motion of the flexure, when a load is applied in this direction. The center of the lower wheel is affixed to the housing of the gauge and constrained against rotation or motion in any direction. The Y-shear arrow corresponds in the same manner, to the arrows showing the motion of the upper wheel. The disk on the top wheel is its center of motion. Figure 3 shows where the optical fibers and strain gauges are located in relation to each wheel. The optical fibers are affixed to the gauge housing and are fixed in relation to the polished counterweights.

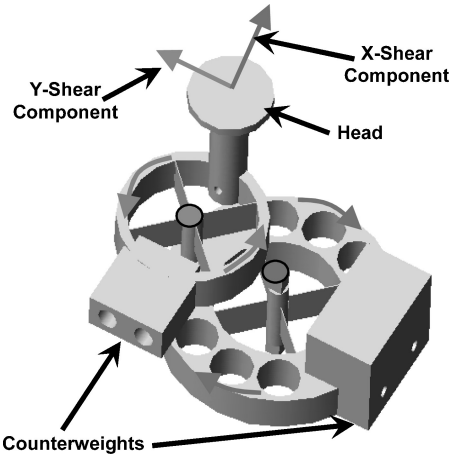

Fig. 2 Two-component wheel gauge schematic.

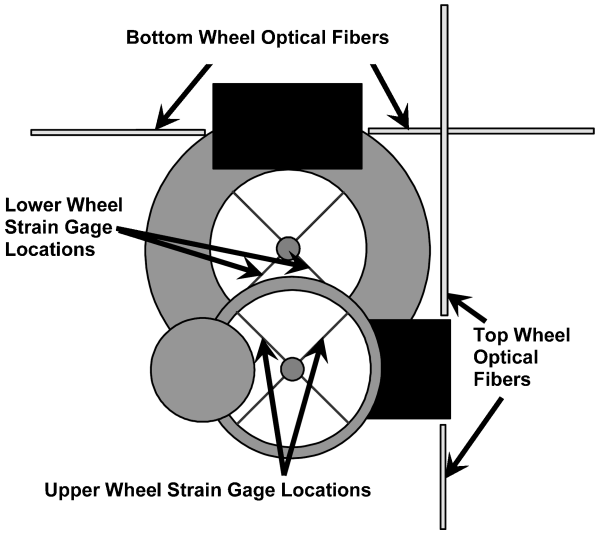

Fig. 3 Top view of gauge and fiber locations.

Material Selection

Haynes® 230® is the material chosen for all of the internal gauge components. This is a high-temperature-strength nickel-based super-alloy, which contains 57% nickel, 22% chromium, 14% tungsten, 5% cobalt, 2% molybdenum, and 3% iron. It resists oxidation up to 1422 K and has a low coefficient of thermal expansion, ranging from 12.7 μm/m · K at 293 K to 16.1 μm/m · K at 1273 K. This material was chosen for its good thermal and mechanical properties as well as for its ability to be machined with conventional techniques. It is used in many high-temperature applications, including the X-43 flight-test vehicle, which uses Haynes 230 as the primary material of the wing structure.[10]

The gold-coated optical fibers define the maximum temperature of the gauge as 1073 K. The bond used to hold the optical fibers to fused silica ferrules and the 316 stainless ferrule holders is made with a silver paste, which has a maximum operating temperature of 1143 K. The metal-foil strain gauges, included for initial validation, are limited to 473 K by the epoxy and solder for the wires. The strain gauges are for calibration purposes only and would not be present on a gauge to be used in very hot flows.

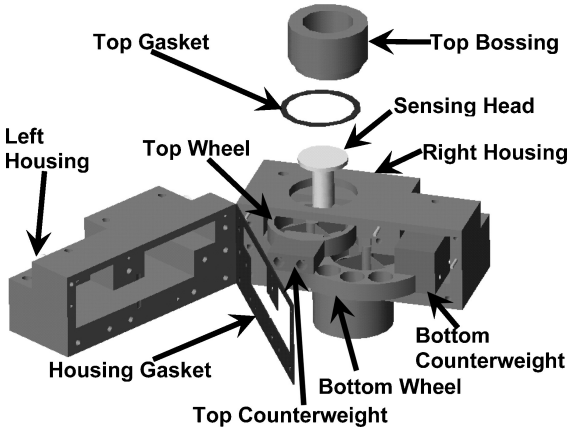

Fig. 4 Open view of wall shear gauge.

Components and Design Features

A drawing of the gauge showing the internal components is in Fig. 4. The wheel spoke flexures are 10 mm long from the center post of the gauge to the inside of the outer ring; they are 140 μ thick and 6 mm deep. The upper wheel is affixed to the lower wheel with a square peg and a small screw. The lower wheel is captured top and bottom, between the two halves of the housing, with a similar arrangement. The round disk on the sensing head is the moving portion of the gauge exposed to the flow. The sensing head is 16 mm in diameter. The top counterweight balances the sensing head mass. The bottom counterweight balances the mass of the top wheel, top counterweight, and the sensing head. Careful balancing of the system proved critical to the success of this gauge.

The sides of the counterweights have an optical finish and serve as the reflectors for the fiber-optic system. The finish was found to hold up to temperatures greater than 1143 K without difficulty. One fiber looks at each side of each counterweight. There is a total of four fibers with two for each component of shear measured. This reduces the temperature sensitivity of the gauge. Any effect of thermal expansion or contraction will be reduced with the redundant measurement of the symmetric displacements.

Fiber-Optic System

Extrinsic Fabry–Perot interferometry (EFPI) relies on the formation of a low-finesse Fabry–Perot cavity in the gap between the end of the fiber and a reflective surface as shown in Fig. 5 (Ref. 11). Some of the laser light is reflected at the end of the fiber and propagates back down to a collector. Then, some of the light traverses the gap, hits an optically reflective surface, and reflects back into the fiber. The resulting fringe pattern can be decomposed to determine the distance between the end of the fiber and the reflector.

Figure 5 illustrates the fiber-optic system used to measure the gap between the fiber and reflector. The outgoing signal is shown in the top right of the figure. The light passes through the sensor, which consists of a fiber with a gap between it and a reflector. The light, which returns to the fiber core, is then measured by a spectrometer, and the resulting fringe pattern is shown in the lower right of Fig. 5 as the returned signal. This signal is then processed with a proprietary Luna Innovations algorithm, and the output is the gap between the fiber and reflector.

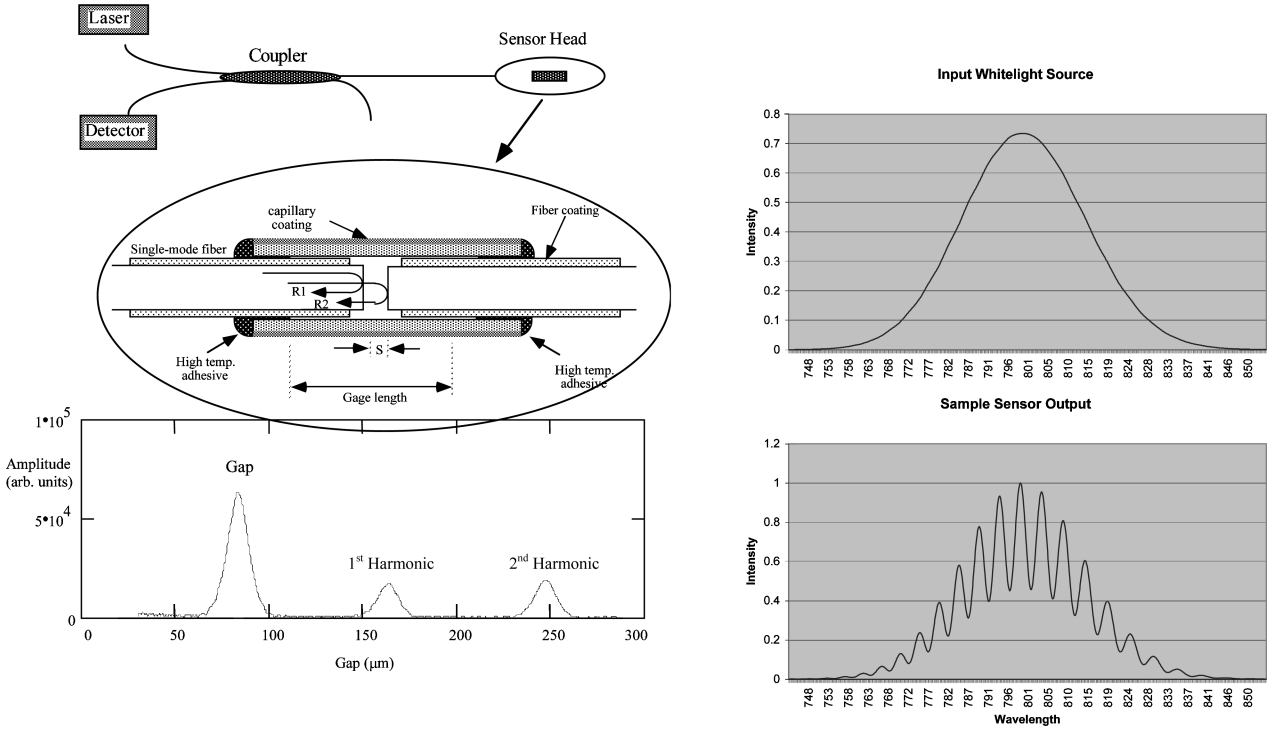

Fig. 5 EFPI system developed by Murphy and coworkers at Luna Innovations, Inc.

Analysis

The finite element method software package ANSYS was used to study various facets of the gauge during the design.

Structural Analysis

The wall shear sensor design process included simple analytic structural tools and extensive use of the ANSYS finite element package. A model internal structure was created to evaluate the displacement of the sensor to a given load. The counterweights are modeled as equivalent masses.

A mesh with 64,721 SOLID 92 elements used in the ANSYS static and modal analysis of the structure is shown in Fig. 6. This element is a 10-node tetrahedron with quadratic displacement behavior. This mesh contains the maximum number of nodes allowed in the version of ANSYS available.

A check of the mesh was run to validate the ANSYS model. In this case the top wheel was held fixed by the support connecting it to the bottom wheel. The result of this sample case was a 12.6-μm displacement at the end of each beam. This compares favorably to the results predicted by a simple beam model of the spokes of the structure, which predicted 12.3 μm. The fine finite element mesh can be expected to be slightly more flexible than the rigid beam theory model.

Figure 7 shows the predicted strain in each of the flexures. The peak strain in each of the bottom spokes is 55.3 microstrains, and this occurs near the fixed pivot of the assembly. This figure shows the effect of a 250-Pa shear load, oriented so that only motion in the lower wheel is produced. The displacements are not to scale. They are exaggerated for clarity in the figures, and this is true for all of the figures generated with ANSYS.

Figure 8 shows the strain on the flexures when the shear is applied in the Y direction. The peak strain is 47.2 microstrains in both the upper and lower wheels. This case shows the cross talk between the two wheels.

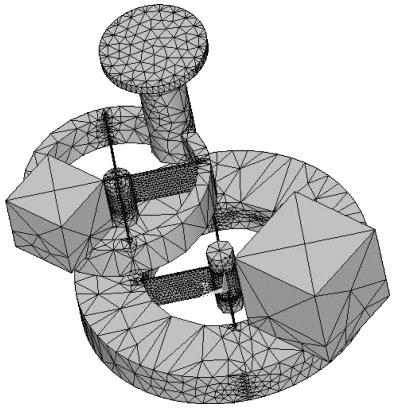

Fig. 6 Static analysis mesh (64,721 elements).

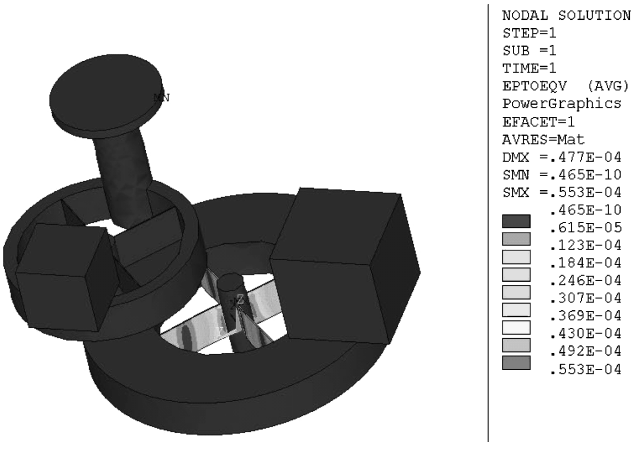

Fig. 7 Analysis results-strain-exciting lower wheel.

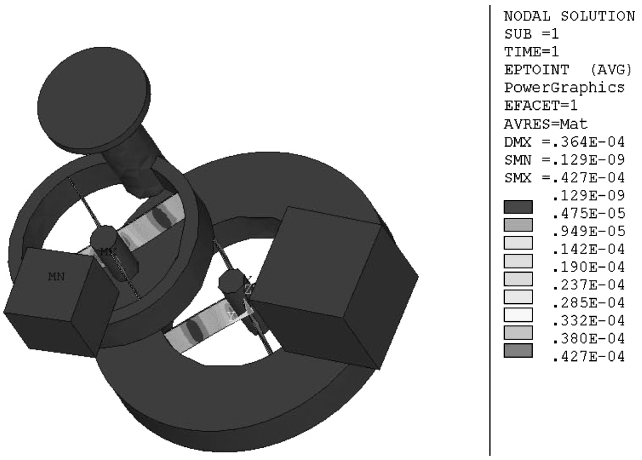

Fig. 8 Analysis results-strain-exciting top wheel.

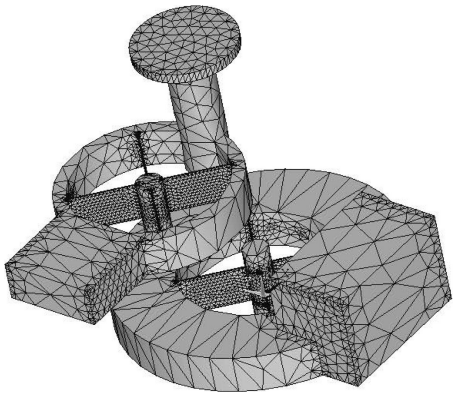

Fig. 9 Mesh with actual couterweights: 55,204 elements.

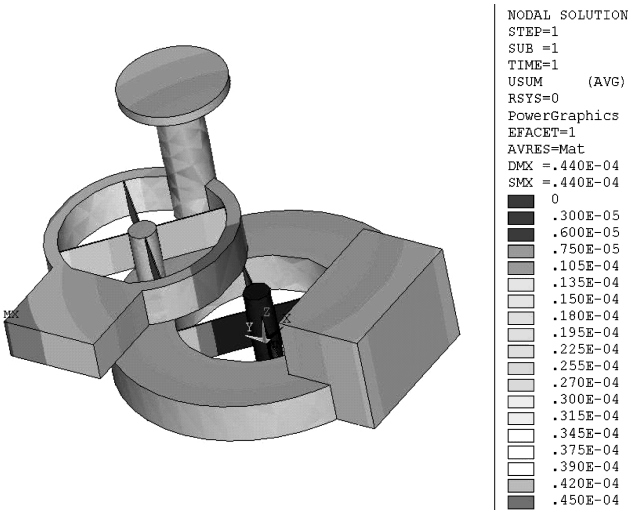

Fig. 10 Total displacements (6-g load on x axis).

Using a model with the actual counterweight geometry, as shown in Fig. 9, allowed the displacements seen by the optical fibers to be calculated. This model has fewer elements than the first mesh because of a change in the shape. The total displacements, as a contour plot, when a 6-g load (corresponding to about 300-Pa shear on the head) is applied to the head of the gauge as a point load in the X direction, are shown in Fig. 10. The Z axis goes up from the X–Y plane and is parallel to the stem of the sensing head. Figure 11 shows a top view of the sensor. The mesh shows the original gauge position and the shaded portion of the figure shows the gauge after the load has been applied. The computed displacements at the fiber-optic

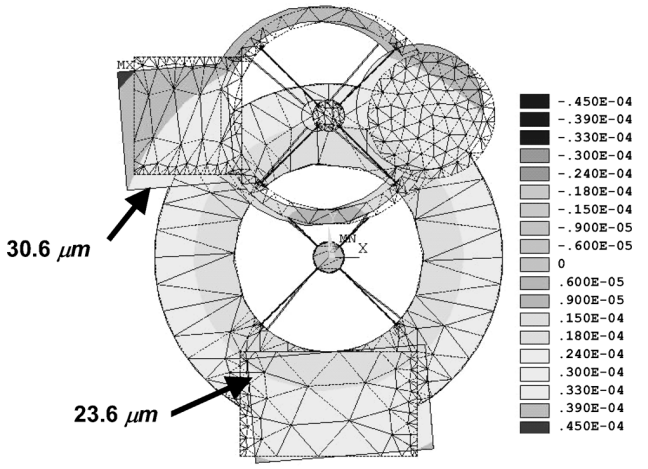

Fig. 11 Top view displacement (meters) measured by fibers (6-g load on *X* axis).

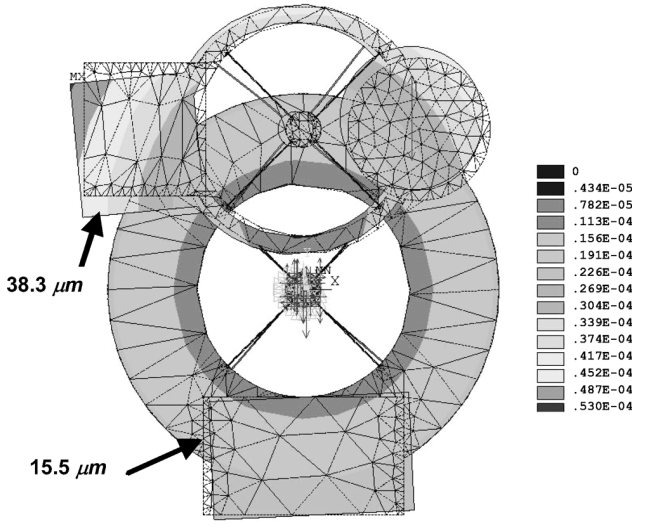

Fig. 12 Top view of total displacement (meters) (6-g load in *Y* direction).

measurement locations are shown with text and arrows. This shows that for a 6-g load in the *X* direction the top wheel will see a change in gap of 30.6 μm and the lower wheel will see a change in gap of 23.6 μm. This also shows that the motions of the wheels are coupled. The strain gauges see a different picture as when the load is only in the *X* direction there is no strain on the webs of the upper wheel. All of the displacement is because the reflector is offset from the center of rotation about the lower wheel, and it sweeps through an arc. The result of this is that the gauge outputs must be put through a calibration matrix, and both the upper and lower wheel data must be known to resolve the two forces from the fiber-optic gap data.

The total displacements of the internal gauge components for a 6-g load in the positive *Y* direction are shown in Fig. 12. The center portion of the lower wheel is constrained against all motion. This is the same condition used for studies of the loads in the direction of the positive *X* axis.

Modal Analysis

A modal analysis was performed in ANSYS to calculate the natural frequencies of the system. This information was used to confirm the results of experimental vibration tests of the gauge and to make sure that the testing environment does not have modes that coincide with those of the gauge. This can lead to problems with the fiber-optic sensors. Figure 13a shows a normal fringe pattern from one of the shear gauge sensors in a quiescent environment, and Fig. 13b shows the degradation of the fiber-optic system measurement with severe vibration. When a large magnitude of vibration occurs, the signal smears, and a gap can no longer be resolved.

Table 1 Modal analysis results

Mode	Frequency, Hz
1	22
2	69
3	442
4	506
5	1138

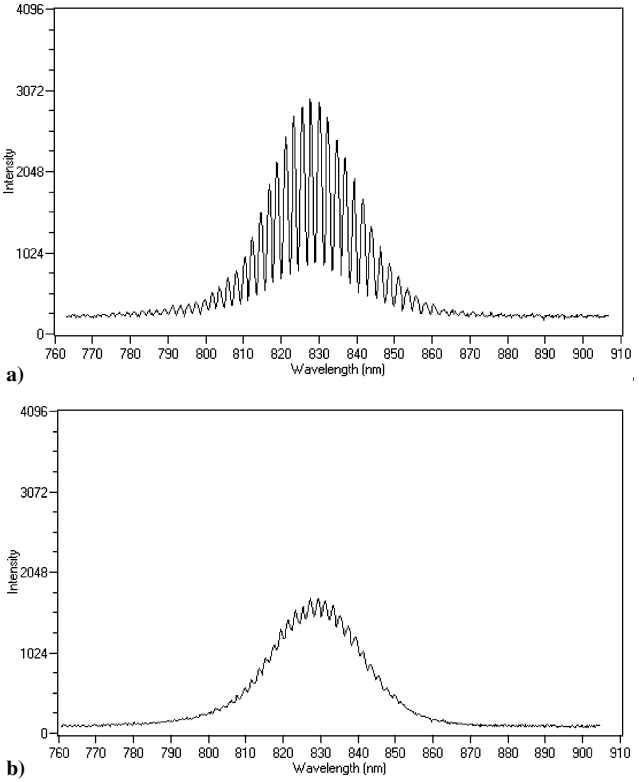

Fig. 13 Raw fiber-optic signal: a) good fringe contrast (no vibration) and b) poor fringe contrast (severe vibration).

The analysis used the same Solid 92 element as the static analysis and the same mesh. In ANSYS, the analysis options were set to solve for the first five mode shapes of the gauge between 0 and 10,000 Hz. The elemental results were calculated, and the default solution method was used. The mode shapes were examined, and there are at least five mesh elements for every half-wavelength for the modes in question. The results of this analysis are shown in Table 1. The major vibration in the Virginia Tech Supersonic Wind Tunnel is much higher than the first two modes of the structure.[7] This means that most of the energy will be used to excite the gauge at the first and second mode and resonance is unlikely to occur.

Thermal Analysis

This gauge is intended for high-temperature applications, requiring a transient thermal analysis to be performed in ANSYS to examine the effects of a high heat flux on the floating head when exposed to the flow. A heat flux of 100,000 W/m^2 was chosen, as it is representative of the level experienced inside of a supersonic combustion ramjet.[9] The Solid 87 thermal element was chosen for the thermal only portion of the analysis. This is a tetrahedron with 10 nodes and is similar to the Solid 92 structural element. It is only applicable to thermal analysis. A verification of the method and mesh was performed with a simple sample problem. This mesh used 64,021 elements and was as fine as possible with the available ANSYS version and is shown in Fig. 14.

The boundary conditions used for this analysis consist of starting the sensor at 300 K with all sides of the sensor insulated (ANSYS default boundary conditions). A steady, uniform heat flux

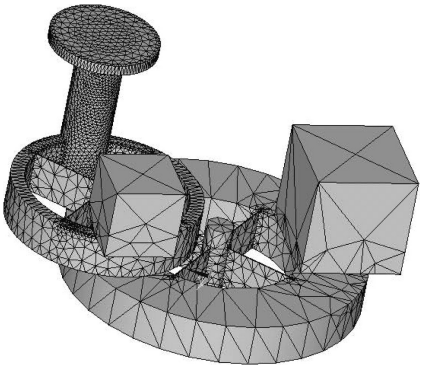

Fig. 14 Mesh for thermal analysis.

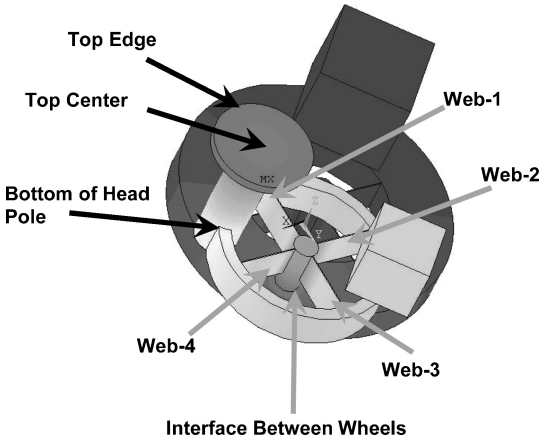

Fig. 15 Node location for time-dependent data.

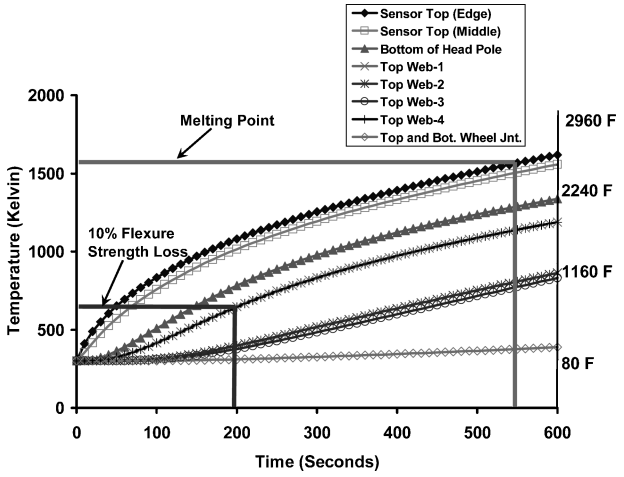

Fig. 16 Temperature of various internal Haynes 230 gauge components vs time.

of 100,000 W/m^2 is applied to the head of the sensor. A running time of 10 min (600 s) heated the head of the sensor to approximately 1500 K. This is considered a good practical limit as the Haynes 230 material melts at around 1600 K.

Figure 15 shows the choice of nodes studied with time-dependent thermal analysis, and Fig. 16 shows the results for various internal gauge components. Figure 16 has two lines labeled: the first line is where the top wheel flexures will experience a 10% drop in strength. This marks where the flexures will begin to be significantly affected by the heat flux. This is predicted to occur after an exposure of 200 s. The second line shows where the head of the gauge would begin to melt. This occurs after about 550 s of exposure. The top wheel heats up faster than the lower wheel as it is closer to the heat source.

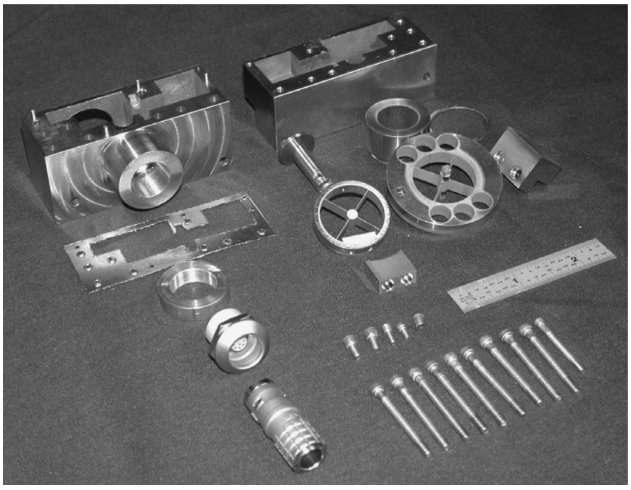

Fig. 17 All gauge parts (scale 2.5 in. long).

The temperature at the junction between the wheels only rises 100 K.

The low thermal expansion characteristics of the Haynes 230 should limit the thermal effects on the lower wheel. This could lead to a greater change in the accuracy of the secondary (Y) component of shear. The secondary component is more dependent on the upper wheel, which is closer to the heat source. In the extreme environment, in which this gauge must operate, this would be an acceptable compromise. If a calibration system can be arranged for these high heat fluxes, the detailed transient thermal behavior of the gauge could be quantified beforehand and the error in measurement reduced.

Gauge Manufacture and Assembly

Conventional machining techniques were used wherever possible. The more critical or difficult operations were performed using electron discharge machining.

All of the gauge components are displayed in Fig. 17. The wheels, counterweights, housing, gaskets, top bossing, connectors, and all of the associated hardware can be seen in this figure. The 0.38-mm-thick graphite gaskets can be seen in the picture for the housing and the top bossing. The gaskets for the strain-gauge connector were created from the same material.

Two webs on each wheel are equipped with the strain gauges. There are two strain gauges on each side of these webs for a total of four gauges per wheel. This creates a full bridge on each wheel and yields the maximum sensitivity. The gauges are mounted near the hub of the wheel where the maximum strain values are predicted to occur.

Calibration

Static calibration involves hanging known masses from the head of the sensor and measuring the resulting displacements and strain-gauge output. The calibration was performed from 0 to 6 g, which is larger than the range of shear expected in cold-flow testing. Repetition of the calibration a number of times yields data on the basic uncertainties of the gauge.

The calibration results are shown in Fig. 18 for the fiber-optic measurements. These data were taken with the Luna Innovations Fast Fiber Scan (FFS) fiber-optic measurement system. The masses were applied in the X-axis direction of the gauge. This figure shows five calibrations superimposed over each other. The calibrations proved linear and repeatable. A linear fit was applied to each channel to determine the corresponding slope.

Figure 19 shows the Y-axis data for all four channels of the FFS system. The strain gauge output was recorded at the same time as the FFS output. The strain-gauge results are shown in Figs. 20 and 21 for the X and Y axes, respectively. There are two separate plots with five calibrations on each. The strain-gauge output comes from

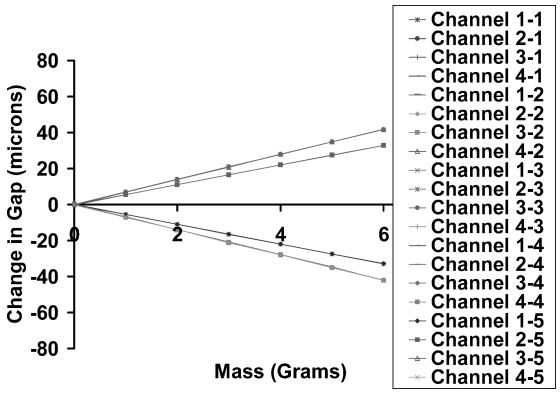

Fig. 18 FFS *X*-axis calibration (five runs).

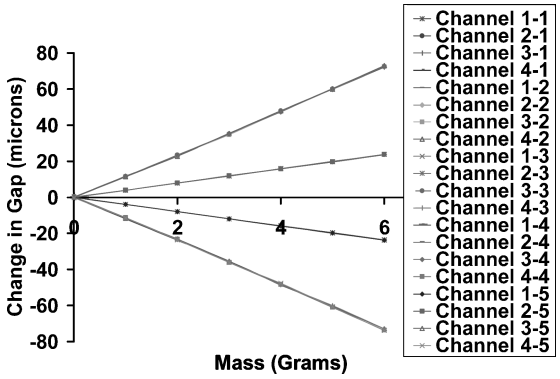

Fig. 19 FFS *Y*-axis calibration (five runs).

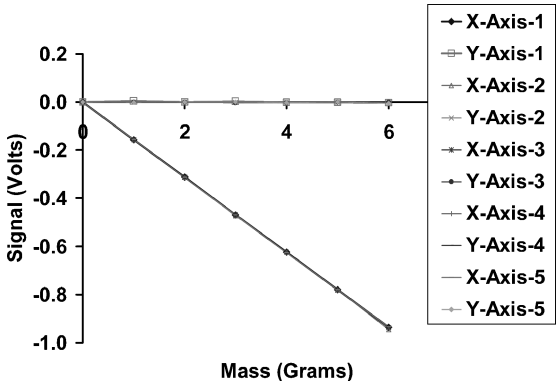

Fig. 20 Strain-gauge *X*-axis calibration (five runs).

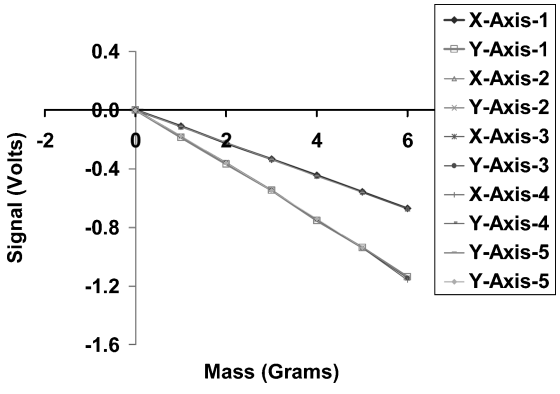

Fig. 21 Strain-gauge *Y*-axis calibration (five runs).

one set of gauges on the upper wheel and one set of gauges on the lower wheels. The output of the lower wheel of this gauge is 0.156 V/g and the upper wheel is 0.191 V/g. The wheels are a coupled system, and the components of shear cannot be separated without the use of both upper-wheel and lower-wheel data at the same point in time.

The general form of the system is shown in Eq. (4). The letter d denotes the displacement or strain from some applied force f, and the subscript denotes the direction. The coordinate system is the previously defined gauge coordinate system. Coefficients c_1 to c_4 are the calibration coefficients. There will be two matrices of coefficients: one for the fiber-optic system and one for the strain-gauge system:

$$\begin{pmatrix} d_x \\ d_y \end{pmatrix} = \begin{bmatrix} c_1 & c_2 \\ c_3 & c_4 \end{bmatrix} \begin{pmatrix} f_x \\ f_y \end{pmatrix} \tag{4}$$

Equation (4) is simply a system of linear equations, and it can be rewritten

$$d_x = f_x c_1 + c_2 f_y \tag{5}$$

$$d_y = f_x c_3 + c_4 f_y \tag{6}$$

When the force is applied only in the X direction, as is the case during the X calibration, the system can be written as Eq. (7). A similar expression can be written for the Y calibration and is shown by Eq. (8):

$$\begin{pmatrix} d_x \\ d_y \end{pmatrix} = \begin{bmatrix} c_1 & c_2 \\ c_3 & c_4 \end{bmatrix} \begin{pmatrix} f_x \\ 0 \end{pmatrix} \tag{7}$$

$$\begin{pmatrix} d_x \\ d_y \end{pmatrix} = \begin{bmatrix} c_1 & c_2 \\ c_3 & c_4 \end{bmatrix} \begin{pmatrix} 0 \\ f_y \end{pmatrix} \tag{8}$$

The result of the calibration is shown in Eq. (9) for the fiber-optic system and in Eq. (10) for the strain-gauge system on the gauge. The coefficient values are for the average of five calibrations. To find the force based on the displacement, each calibration matrix must have an inverse and therefore be nonsingular. The determinate of both matrices are nonzero and therefore they are nonsingular and invertible[12]:

$$C_{\mathrm{FO}} = \begin{bmatrix} 5.48761 & 3.95073 \\ 6.99156 & 12.1822 \end{bmatrix}, \qquad |C_{\mathrm{FO}}| = 39.229 \tag{9}$$

$$C_{\mathrm{SG}} = \begin{bmatrix} -0.15622 & -0.11224 \\ -0.00046 & -0.19058 \end{bmatrix}, \qquad |C_{\mathrm{SG}}| = 0.29824 \tag{10}$$

Equation (11) simply states that the inverse of the calibration matrix multiplied by the displacements recorded by the gauge will result in the applied force.

$$\boldsymbol{f} = C^{-1}\boldsymbol{d} \tag{11}$$

To check the validity of the calibration matrix, angular calibration data, where loads were applied at a 45-deg angle to the X axis, were used. Five calibrations were performed, and the average values input into the calibration matrix. The output results for the fiber-optic system and the strain-gauge measurement systems are shown in Fig. 22. This shows excellent agreement between the X and Y data for both measurement systems.

This 45-deg condition is where the error should be a maximum as the coefficients are computed when only a pure X or Y force is applied. The maximum error noted for this figure is a 12% overestimate of the shear force, for small forces. This decreases to a maximum error of 7% at a load of 6 g, which corresponds to a shear of 300 Pa. These errors will decrease for smaller angles; when the forces are perfectly aligned with the X and Y gauge axes, the errors approach zero, as the calibration coefficients were created with these cases.

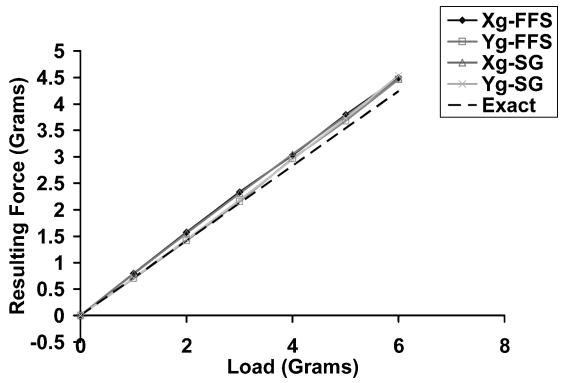

Fig. 22 Reduced strain-gauge and fiber-optic angular calibration data.

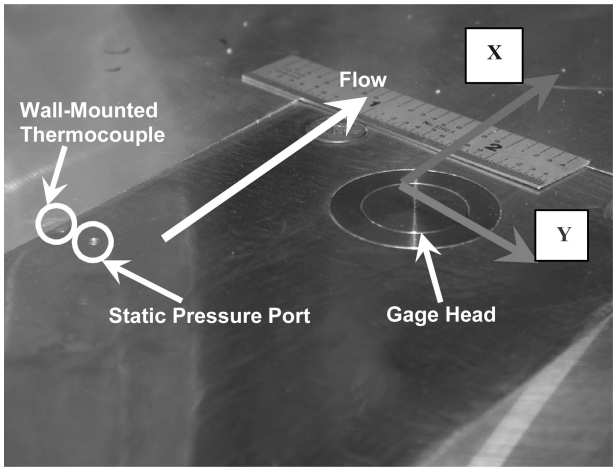

Fig. 23 Gauge in tunnel with instrumentation.

Wind-Tunnel Tests

Wind-Tunnel Facilities and Instrumentation

The gauge was tested in the Virginia Tech Supersonic Wind Tunnel (SSWT). The facility is a blowdown, cold-flow ($T_0 \sim 300$ K) tunnel with nominal test duration of approximately 10 s. Normal test conditions are a total pressure of 3.4 atm (~50 psia) at Mach 2.4 ($Re = 6.6 \times 10^7$/m) and 10.2 atm (~150 psia) at Mach 4.0 ($Re = 7.4 \times 10^7$/m) with a total temperature of 300 K. The test section is 23 × 23 cm in cross section. A Haynes 230 insert is used so that the thermal properties of the surrounding wall match the head and housing of the sensor.

This facility allows the gauge to be exposed to a shear of approximately 150–300 Pa, at Mach 2.4, depending on the total pressure in the tunnel. The setup and equipment is the same for the Mach 4.0 tests except for the Mach 4.0 nozzle block.

Figure 23 shows the Haynes 230 floor plate with the sensor head in the test section. The locations of the static-pressure port and wall-mounted Medtherm thermocouple are also shown. These devices are upstream of the gauge head and off to one side so that they do not disturb the flow over the gauge head.

Experimental Modal Results

The modes and damping ratio were calculated from the free response of the structure after the tunnel unstarted. The tunnel is a steady vibration environment during the run, and the start and unstart provide large impulses. The experimental frequency of the first mode is 18.9 Hz. This is 14% less than the predicted value of 22 Hz. This discrepancy is not unexpected because the 140-μm (0.00551-in.)-thick webs have a machining tolerance of about ± 10 μm (0.0004 in.), and the webs also have strain gauges affixed with all of the associated glue, wires, and solder pads. The upper-wheel data confirm the 18.9-Hz first mode and also show the second mode at 47.5 Hz. The finite element analysis prediction of the second mode was 69 Hz. The damping ratio of the structure can be computed using Eq. (12) (Ref. 13). The resulting damping ratio is $\zeta_L = 0.00109$ for the lower wheel. The upper wheel yields $\zeta_u = 0.00144$. Equation (13) shows the expression to calculate the undamped natural frequency ϖ_n from the damping ratio and the damped natural frequency ϖ_d. Because of the very small values of ζ, for this structure ϖ_n and ϖ_d are essentially the same. A summary of the results for the frequency and damping data is shown in Table 2:

Table 2 Summary of frequency results

Wheel	Calculated ϖ_n, Hz	ϖ_d, HZ	ϖ_n, Hz	% Difference	ζ
Lower	22	18.9	18.9	−16.4	0.00109
Upper	69	47.5	47.5	−31.2	0.00144

$$\zeta = \frac{[1/(n-1)][\ell_n(A_1/A_n)]}{\sqrt{4\pi^2 + \{[1/(n-1)][\ell_n(A_1/A_n)]\}^2}} \tag{12}$$

$$\omega_d = \omega_n \sqrt{1-\zeta^2} \tag{13}$$

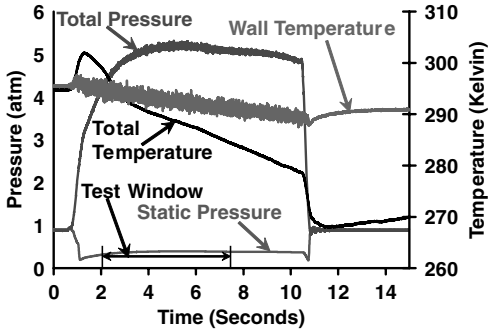

Fig. 24 The 10-23-03 run-1 $M = 2.4$ tunnel conditions.

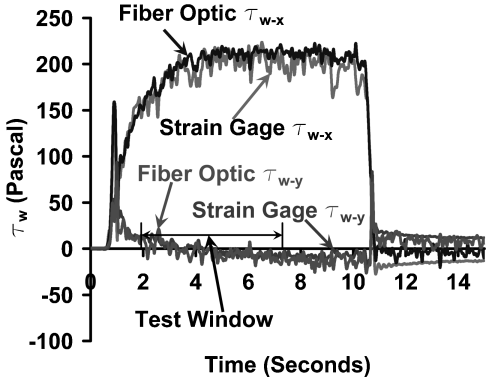

Fig. 25 The 10-23-03 run-1 $M = 2.4$ wall shear components.

Mach 2.4 Results

The flow conditions in the wind tunnel are shown in Fig. 24. There is a "test window" labeled in the figure and in all subsequent figures for the test. This is the region considered steady state for the purposes of comparing the results. This yields an approximate 6 s of steady-state time for each 8-s SSWT test. The computed Mach number is 2.34 with the nominal Mach number for the tunnel being 2.4. The skin-friction results are shown in Figs. 24–26 for the case where the gauge X axis is aligned with the streamwise flow.

The actual flow in the SSWT is nominally two-dimensional, and so the gauge axis was next purposefully misaligned by 25 deg to the flow. This created a flow that appeared three-dimensional to the gauge. Table 3 shows the error in flow angle, relative to the gauge

Table 3 Error in angular shear data

Method	Total shear, Pa	X shear, Pa	Y shear, Pa	Calculated angle, deg	Error from 25 deg, deg
Strain gauge	163	152	66	23.5	1.5
Fiber optic	174	164	62	20.7	4.3

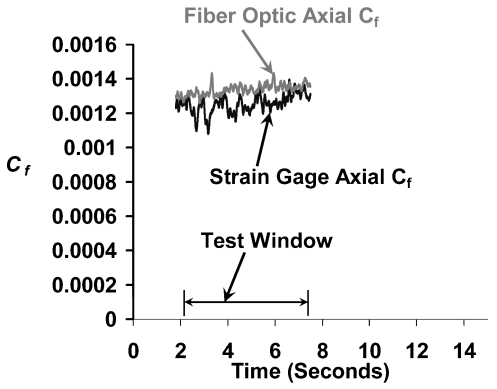

Fig. 26 The 10-23-03 run-1 $M = 2.4$ C_f.

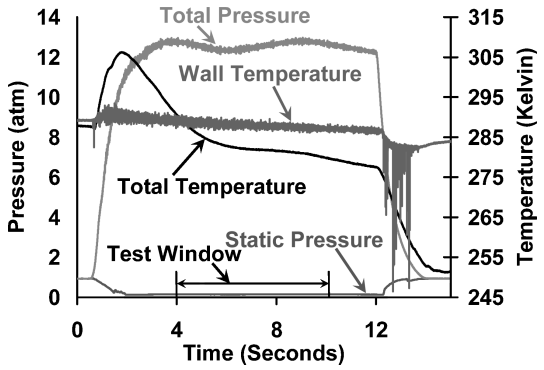

Fig. 27 The 12-13-03 run-13 $M = 4.0$ tunnel conditions.

coordinate system for both the strain-gauge and fiber-optic data. The flow angle is calculated from the X and Y shear components, with the assumption that the flow is essentially two dimensional and the shear is down the X direction of the tunnel coordinate system. The error in the flow angle computed with the fiber-optic data is slightly greater than the computed strain-gauge flow angle. The larger error in the fiber-optic angle is likely because of the higher dependence between the wheels for displacement-based shear component computation.

Mach 4.0 Results

The total pressures at Mach 4.0 are approximately 13 atm, as opposed to about 4.5 atm at Mach 2.4. The actual calculated Mach number was 3.62 from the total pressure and static pressure. The tunnel control was somewhat more inconsistent at Mach 4.0 and more sensitive to changes in settings than at Mach 2.4. This likely contributes to measurement uncertainty. The results for the Mach 4.0 case are shown in Figs. 27–29. The main items to note are that the gauge was kept aligned with the flow for all of the Mach 4.0 cases and that 32 runs were performed.

Boundary-Layer Survey Results

The boundary-layer survey is needed to measure the boundary-layer thickness in the supersonic tunnel at the various total pressures tested during the wall shear measurements. This was accomplished using a traverse with pitot, total temperature, and cone-static probes.

The boundary-layer thickness is used to calculate a Reynolds number based on the boundary-layer thickness:

$$Re_\delta = \rho U \delta / \mu \tag{14}$$

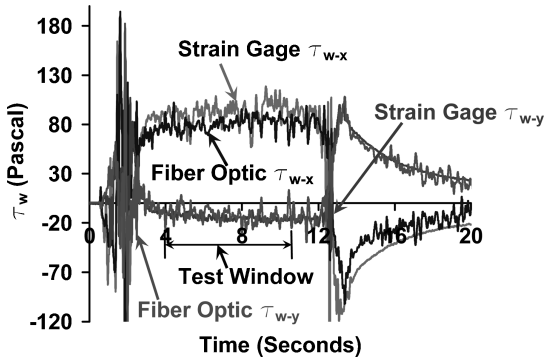

Fig. 28 The 12-13-03 run-13 $M = 4.0$ wall shear components.

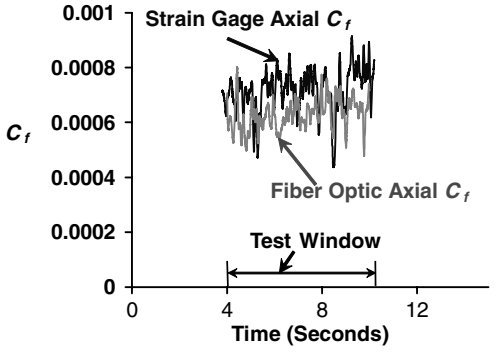

Fig. 29 The 12-13-03 run-13 $M = 4.0$ C_f.

This information is used in Eq. (15):

$$\sqrt{2/C_f} = A \log\left(Re_\delta \sqrt{C_f/2}\right) + C - B \tag{15}$$

with

$$A = 5.6, \qquad B = -2.5, \qquad C = 4.9$$

The incompressible-to-compressible correction factors for C_f, Van Driest II are shown in Eq. (16) (Ref. 1):

$$C_{f,\text{compr}}/C_{f,\text{incompr}} = 0.66 \rightarrow (\text{Mach } 2.4)$$

$$C_{f,\text{compr}}/C_{f,\text{incompr}} = 0.50 \rightarrow (\text{Mach } 4.0) \tag{16}$$

There are many methods of computing the incompressible-to-compressible correction factor, and another technique is the reference temperature method. Equation (17) shows the needed expressions from Ref. 14. The Prandtl number is assumed to be 0.7 for air. For Mach 2.4 this yields a correction factor of 0.686, and for Mach 4.0 the factor is 0.477. These agree quite well when compared to the results shown in Eq. (16). Both C_f prediction methods are shown with the final results in Figs. 30 and 31:

$$C_{f,\text{compr}}/C_{f,\text{incompr}} = \{1 + r[(\gamma - 1)/4]M^2\}^{-1}, \qquad r = \sqrt{pr} \tag{17}$$

The results for C_f predicted using the the boundary-layer survey data for Mach 2.4 are shown in Fig. 30, along with the experimentally determined values of C_f for both the strain gauges and the fiber-optic data-acquisition system. The results are plotted as a function of the total pressure. The Van Driest II incompressible-to-compressible factor predicts a slightly lower skin-friction coefficient value when compared with the reference temperature method at Mach 2.4. The gauge values fall in a range that encompasses both values. The fiber-optic system tends to predict a higher skin-friction coefficient at Mach 2.4 than the strain-gauge system. The agreement between the direct C_f measurement and the semiempirical C_f prediction is very good, as might be expected for a simple, flat-plate flow. This represents a critical step in the validation process for the gauge.

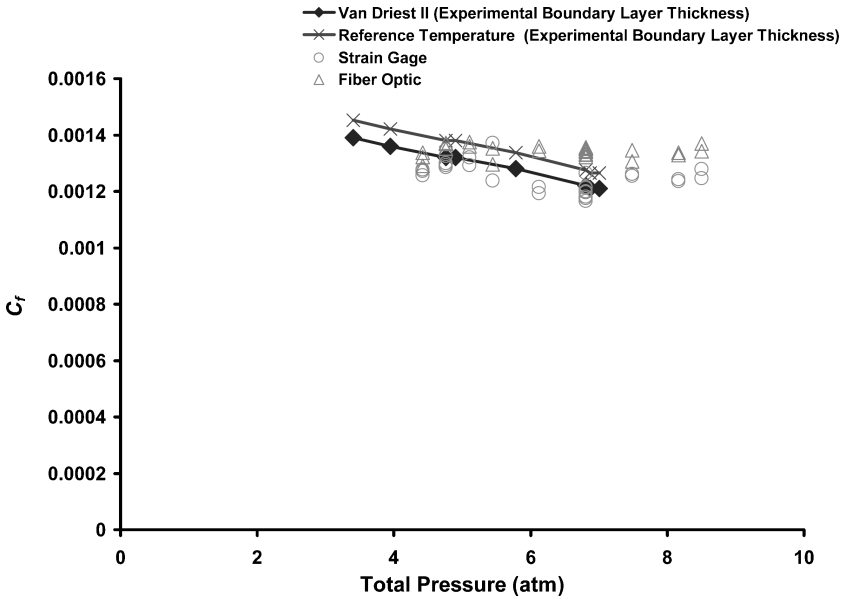

Fig. 30 Boundary-layer survey predicted C_f and gauge values at Mach 2.4.

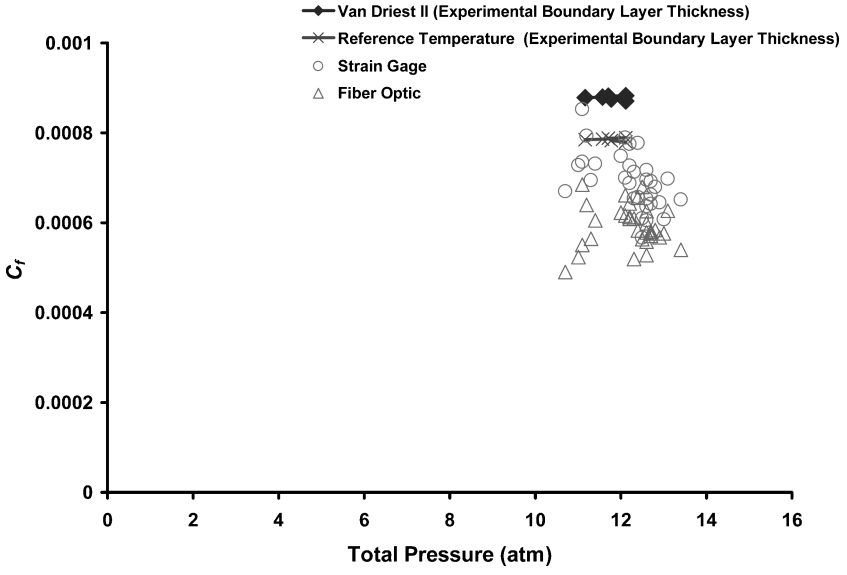

Fig. 31 Boundary-layer survey predicted C_f and gauge values at Mach 4.0.

Table 4 Semiempirical results compared with gauge results [% of FS: 10 g (500 Pa)]

	Mach 2.4		Mach 4.0	
Method	Van Driest II	Reference temperature	Van Driest II	Reference temperature
Fiber optic	±6% FS	±4% FS	−7% FS	−5% FS
Strain gauge	±4% FS	±5% FS	−4% FS	±1% FS

The results of the boundary-layer survey at Mach 3.62 (Mach 4.0 nominal) are shown in Fig. 31. The skin-friction coefficient is noticeably lower at Mach 4, with a value of about 0.0007, compared with about 0.0013 at Mach 2.4. The strain gauges predicted a consistently higher C_f value than the fiber-optic system at Mach 4.0. Both measurements were lower than the predicted value. This could mean that the prediction methods do not work quite as well at Mach 4.0. There appears to be a larger deviation in the data from the mean relative to the magnitude of the signal. This is likely because of the smaller shear values at Mach 4.0 and the smaller signal-to-noise ratio.

A comparison of the semiempirical results to the values measured with the gauge is shown in Table 4. The Van Driest II incompressible-to-compressible factor predicts a higher lower skin-friction coefficient value when compared with the reference temperature method at Mach 4.0. At Mach 4.0 the spread between the two semiempirical prediction methods is greater. The gauge data agree more closely with the reference temperature method.

Uncertainties

An obvious area of uncertainty is the design of the floating head and gap. Closely related are the uncertainties from any misalignment of the head with the adjacent wall. Measurements for a few sets of conditions have been published, which provide the gauge designer with useful information on how to minimize errors. The limitation to the available experimental results is that they are for a few particular cases that might or might not be applicable to a new gauge design condition. For example, the helpful results of Allen (1980) were obtained for a nulling gauge with a large floating head (127-mm diam) in an unheated supersonic flow ($M = 2.2$) (Ref. 15). How should they be applied to a low-speed case or a hot, hypersonic flow with a much smaller head size compared to the local boundary-layer thickness? The only study of these issues with modern computational fluid dynamics (CFD) tools is MacLean and Schetz.[16] They considered low-speed turbulent flow at $Re_x = 2 \times 10^6$. CFD is attractive because calculations can be made for any projected set

Table 5 Error and uncertainty summary [% FS: 10 g (500 Pa)]

Type of uncertainty	Strain gauge	Fiber optic
Head lip size	±1% FS	±1% FS
Head protrusion	±1% FS	±1% FS
Head/housing gap	±1.9% FS	±1.9% FS
Total head effect uncertainty	±2.4% FS	±2.4% FS
2σ Uncertainty in calibration	±6.3% FS	±6.2% FS
2σ Uncertainty in $M = 2.4$ C_f (28 runs)	±4.1% FS	±1.6% FS
2σ Uncertainty in $M = 4.0$ C_f (32 runs)	±2.6% FS	±2.3% FS

of conditions and geometry. Putting this all together, the designer can use experimental information and/or CFD tools to design skin-friction gauges, where the errors caused by head design, gap size, and reasonable misalignment can be limited to about ±2%.

The effects of an axial pressure gradient on a skin-friction gauge are a concern, and experiments suggest that small lip thickness and small gaps help to minimize such influences. Also, one of the intended benefits of a liquid fill in the housing is to minimize pressure gradient effects. The idea is that low internal velocities of an incompressible fluid cannot produce large static-pressure variations. Supersonic flows can have very large pressure gradients, especially across shocks, and there has not been a definitive experimental study for the supersonic flow regime. Again, CFD would seem to be a good approach to pressure gradient issues for all regimes; some CFD results are available in MacLean and Schetz, where pressure gradients were created by imposing a virtual diverging or converging channel above the gauge.[16]

For hot-flow conditions, the biggest uncertainty is surely the result of unsteady and/or spatially nonuniform temperature variations. With careful design, at Virginia Tech we have conducted tests under very hot flow conditions for a few seconds where estimated errors from temperature were kept to about ±10%.

A very crude summary of the uncertainty for direct skin-friction measurements including gauge design, calibration, pressure, and temperature might be 1) unheated subsonic and supersonic flows without shocks impinging on the gauge about ±5–10%, 2) hot subsonic and supersonic flows without shocks impinging on the gauge about ±10–20%, and 3) supersonic flows with shocks impinging on the gauge have uncertainties too large to be useful.

Applying the available experimental and CFD results from the literature, we have uncertainty estimates for the current gauge. The results are summarized in Table 5. The first four rows in the table show the effect of misalignment errors of the head on the final results. The total error expected from the geometry is only about ±2.4%, using the methods of MacLean and Schetz.[16] The predicted uncertainty caused by the head geometry is acceptably small.

The uncertainty in C_f, measured in the SSWT at Mach 2.4, is less than the calibration uncertainty recorded. The uncertainty in the fiber-optic measurement was lower than the strain gauges for both the Mach 2.4 and the Mach 4.0 conditions. The uncertainties shown in Table 5 are based on the full-scale deflection of the gauge at 500 Pa. The magnitude of the uncertainties at Mach 2.4 are ±1.6% full-scale (FS) (±8 Pa) for the fiber-optic data and ±4.1% FS (±21 Pa) for the strain gauge data. At Mach 4.0 the uncertainties are ±2.3% FS (±12 Pa) for the fiber optics and ±2.6% FS (±13 Pa) for the strain gauges.

Summary

This design, analysis, calibration, and cold-flow testing of this shear gauge have shown the validity of the two-wheel flexure design concept. A workable two-component fiber-optic wall shear gauge can be made without the use of viscous damping fluids.

Finite element analysis proved a useful design tool, and the gauge generally behaved as predicted. Statically, the basic behavior was in line with predictions even though there was some error in the magnitudes of the values. The geometry modeled and the actually geometry of the flexures were not identical because of manufacturing tolerances. Modal analysis results were within 16.4% for the first mode measured as 18.9 Hz and within 30% for the second mode, which was measured as 47.5 Hz. The thermal analysis predicts that the gauge is capable of surviving up to 10 min of a very high heat flux and should be able to operate for up to 3 min with only a 10% change in the stiffness of the upper-wheel flexures.

Table 6 Summary of gauge performance with 16-mm-diam head

Quantity	Strain gauge	Fiber optic
Sensitivity X axis	0.156 V/g (0.00312 V/Pa)	5.5 μm/g (0.110 μm/Pa)
Sensitivity Y axis	0.191 V/g (0.00382 V/Pa)	12.2 μm/g (0.244 μm/Pa)
Dynamic range (total shear)	0–10 g (0–500 Pa)	0–10 g (0–500 Pa)
Sampling frequency	100 Hz	500 Hz

Repeated calibrations demonstrate the linear and repeatable output of the gauge. Uncertainties in the calibration are about ±6% for both the strain gauges and the fiber-optic systems.

Wind-tunnel tests at Mach 2.4 and Mach 4.0 under high-Reynolds-number conditions showed the durability of this wall shear gauge in addition to the repeatability of its measurements. The 2σ uncertainties at Mach 2.4 are ±1.6% FS for the fiber-optic data and ±4.1% FS for the strain-gauge data. At Mach 4.0 the uncertainties are acceptably low with ±2.3% FS for the fiber optics and ±2.6% FS for the strain gauges. The performance specifications of the gauge are summarized in Table 6.

Acknowledgments

This research was supported by a contract from NASA Dryden Flight Research Center.

References

[1]Schetz, J. A., *Boundary Layer Analysis*, Prentice–Hall, Englewood Cliffs, NJ, 1993, pp. 206–214, 420–426.

[2]Nitsche, W., Haberland, C., and Thunker, R., "Comparative Investigations of the Friction Drag Measuring Techniques in Experimental Aerodynamics," *International Council of the Aeronautical Sciences Congress,* Vol. 14, edited by B. Laschka and R. Staufenbiel, 1984, pp. 391–403.

[3]Winter, K., "An Outline of the Techniques Available for the Measurement of Skin Friction in Turbulent Boundary Layers," *Progress in Aerospace Science*, Vol. 18, No. 1, 1977, pp. 1–57.

[4]Schetz, J. A., "Direct Measurements of Skin Friction in Complex Flows," *Applied Mechanical Reviews*, Vol. 50, No. 11, Pt. 2, 1997, pp. S198–S203.

[5]Chadwick, K., DeTurris, D. J., and Schetz, J. A., "Direct Measurements of Skin Friction in Supersonic Combustion Flowfields," *Journal of Engineering for Gas Turbines and Power*, Vol. 115, No. 3, 1993, pp. 507–514.

[6]Pulliam, W. J., and Schetz, J. A., "Development of Fiber Optic Sensors for High Reynolds Number Supersonic Flows," AIAA Paper 2001-0245, Jan. 2001.

[7]Remington, A., and Schetz, J. A., "A Study of Magnetically Damped Skin Friction Measurements for High Vibration Environments," AIAA Paper 2000-2522, June 2000.

[8]Sang, A., and Schetz, J., "Study of Rubber Damped Skin Friction Gauges for Transonic Flight Testing," AIAA Paper 2002-0533, Jan. 2002.

[9]Smith, T. B., Schetz, J. A., and Bui, T., "Development of Direct-Measuring Skin Friction Gauges for Hypersonic Flight Tests," *AIAA Journal*, Vol. 41, No. 8, 2003, pp. 1429–1437.

[10]Ko, W., and Gong, L., "Thermostructural Analysis of Unconventional Wing Structures of Hyper-X Hypersonic Flight Research Vehicle for the Mach 7 Mission," NASA TP-2001-210398, Oct. 2001.

[11]Murphy, K., Gunther, M., Vengsarkar, A., and Claus, R. O., "Quadrature Phase-Shifted, Extrinsic Fabry–Perot Optical Fiber Sensors," *Optics Letters*, Vol. 16, No. 4, 1991, pp. 273–275.

[12]O'Neil, P., *Advanced Engineering Mathematics*, 4th ed., PWS Publishing, Boston, 1995, pp. 372–391.

[13]Ogata, K., *System Dynamics*, 3rd ed., Prentice–Hall, Upper Saddle River, 1998, pp. 244–248.

[14]Schlichting, H., and Gersten, K., *Boundary Layer Theory*, 8th ed., Springer-Verlag, New York, 2000.

[15]Allen, J. M., "Improved Sensing Element for Skin-Friction Balance Measurements," *AIAA Journal*, Vol. 18, No. 11, 1980, pp. 1342–1345.

[16]MacLean, M., and Schetz, J. A., "Numerical Detailed Study of Flow Affecting a Direct Measuring Skin Friction Gauge," *AIAA Journal*, Vol. 41, No. 7, 2003, pp. 1271–1281.

R. Lucht
Associate Editor